

# Quantum simulations of localization effects with dipolar interactions

Gonzalo A. Álvarez<sup>1,2,\*</sup>, Robin Kaiser<sup>3</sup>, and Dieter Suter<sup>2</sup>

Received 29 April 2013, revised 22 August 2013, accepted 6 September 2013

Published online 11 October 2013

Quantum information processing often uses systems with dipolar interactions. Here a nuclear spin-based quantum simulator is used to study the spreading of information in such a dipolar-coupled system. While the information spreads with no apparent limits in the case of ideal dipolar couplings, additional perturbations limit the spreading, leading to localization. In previous work [Phys. Rev. Lett. **104**, 230403 (2010)], it was found that the system size reaches a dynamic equilibrium that decreases with the square of the perturbation strength. This work examines the impact of a disordered Hamiltonian with dipolar  $1/r^3$  interactions. It shows that the expansion of the cluster of spins freezes in the presence of large disorder, reminiscent of Anderson localization of non-interacting waves in a disordered potential.

## 1 Introduction

The control of quantum mechanical systems has continued to attract interest in recent years [1–8], mainly triggered by the pursuit of quantum information processing and quantum simulations, both of which have the potential for solving computational problems more efficiently than classical computers [9–11]. The realization of this potential requires precise control of large quantum systems [12]. Controlling small quantum systems has been explored extensively over the last few years [1–8, 13], but control of large quantum systems is still very challenging. The simulation of large quantum systems using classical computers is limited to about 20 qubits if only pure states are considered [14, 15]. The typical classical algorithms can also be extended to calculate the dynamics of mixed states if the initial state or the observables are localized in a region smaller than the complete system. This approach uses quantum parallelism of a single pure state evolution [16, 17]. Present quantum technologies do not allow complete control of large

quantum states. Large quantum systems of thousands of qubits have been used for ensemble quantum simulations in nuclear magnetic resonance (NMR) experiments on solid-state systems [18–20] and with beryllium ions stored in a Penning trap [21], and superconducting flux qubits [22, 23].

The main difficulties for controlling large quantum systems are the lack of individual addressing of qubits, with important efforts in progress using samples of ultracold atoms [24, 25]. For large systems, decoherence is known to degrade the information contained in the quantum state [26]. Its rate increases with the size of the quantum system, making the largest systems the most susceptible to perturbations [13, 18, 19, 27–32]. While these effects are known to affect the survival time of quantum information, they also affect the distance over which quantum states can be transmitted [20, 32–41]. Imperfections or disorder of the spin–spin couplings that drive state transfer can induce localization of quantum information [33, 35, 36, 38] in a process related to Anderson localization [42, 43]. Whereas disorder-induced inhibition of transport of non-interacting waves has been studied in various physical systems [44–48], the role of dipolar interactions is under theoretical investigation [49]. Here we study a three-dimensional spin network and demonstrate experimentally a similar behavior by studying the localization effects induced by the finite precision of quantum gate operations used for transferring quantum states [20, 39].

Reducing decoherence is a main step towards implementing large-scale quantum computers. Several techniques have been proposed for this purpose, including dynamical decoupling [50], decoherence-free

\* Corresponding author E-mail: gonzalo.a.alvarez@weizmann.ac.il

<sup>1</sup> Department of Chemical Physics, Weizmann Institute of Science, Rehovot, 76100, Israel

<sup>2</sup> Fakultät Physik, Technische Universität Dortmund, D-44221, Dortmund, Germany

<sup>3</sup> Université de Nice Sophia Antipolis, CNRS, Institut Non-Lineaire de Nice, France

subspaces [51], and quantum error correction [52, 53]. These methods perform very well for small quantum systems [54–60], but they can be very challenging to implement in large quantum systems. However, based only on global manipulations of spins, some of these methods were successfully implemented in large quantum systems with thousands of qubits [19, 30, 31]. The decoherence times were extended by almost two orders of magnitude. Therefore, understanding the decoherence effects and their sources on large quantum systems would help in the optimization of the techniques for controlling decoherence.

In this paper, we focus on understanding the impact of perturbations with dipolar disorder on large quantum systems using quantum simulations with solid-state nuclear spin systems. These interactions depend on the distance  $r$  between the spins as  $1/r^3$ . In particular we study the length scale of localization induced by perturbing the Hamiltonian that drives the spreading of information. Based on our previous results and methods developed earlier [20, 39], we prepared a system of nuclear spins  $1/2$ . Starting with uncorrelated spins we let them evolve into clusters of correlated spins with increasing size. By introducing a controlled perturbation to the Hamiltonian that generates these clusters, we find that the size of the system tends towards a limiting value determined by a dynamic equilibrium [20, 39]: if the cluster size is initially larger than this equilibrium value, it decreases under the effect of the perturbed Hamiltonian, and it increases while its size is below the stationary value. The equilibrium size decreases with increasing strength of the perturbation.

The paper is organized as follows. Section 2 describes the quantum simulator, both the system and the preparation of the initial state. Section 3 describes the quantum simulations. It is divided into two parts. Section 3.1 describes the unperturbed evolutions that drive the growth of the clusters, and it describes the technique for measuring the size of the clusters. In Section 3.2 we discuss the perturbed evolutions, and describe the perturbations and how we create them. In Section 3.3 we discuss the dynamical equilibrium with stationary cluster size, which is independent of the initial states with different cluster sizes. Lastly, Section 4 contains the conclusions.

## 2 The quantum simulator

### 2.1 System

We consider a system of equivalent spins  $I = 1/2$  in the presence of a strong magnetic field and subject to mu-

tual dipole–dipole interaction. The Hamiltonian of the system is

$$\hat{\mathcal{H}} = \hat{\mathcal{H}}_z + \hat{\mathcal{H}}_{\text{dip}}, \quad (1)$$

where  $\hat{\mathcal{H}}_z = \omega_z \sum_i \hat{I}_z^i$  represents the Zeeman interaction with  $\omega_z = \hbar\gamma B_0$  as the Larmor frequency, and

$$\hat{\mathcal{H}}_{\text{dip}} = \frac{1}{2} \sum_{i < j} \frac{\vec{\mu}_i \cdot \vec{\mu}_j}{r_{ij}^3} - \frac{3(\vec{\mu}_i \cdot \vec{r}_{ij})(\vec{\mu}_j \cdot \vec{r}_{ij})}{r_{ij}^5} \quad (2)$$

is the dipolar interaction [61], typically found also in dipolar quantum gases [62] and Rydberg atoms [63] of growing interest in the context of quantum information science. The dipoles are  $\vec{\mu}_i = \hbar\gamma(\hat{I}_x^i, \hat{I}_y^i, \hat{I}_z^i)$  with  $\hat{I}_x^i, \hat{I}_y^i$  and  $\hat{I}_z^i$  the spin operators and  $\vec{r}_{ij}$  is the distance vector between  $\vec{\mu}_i$  and  $\vec{\mu}_j$ . In the presence of a strong magnetic field ( $\omega_z \gg d_{ij}$ ), it is possible to truncate  $\hat{\mathcal{H}}_{\text{dip}}$  with respect to  $\hat{\mathcal{H}}_z$ . The part that does not commute has negligible effect on the evolution of the system [61], while the secular part can be written as

$$\hat{\mathcal{H}}_{\text{dd}} = \sum_{i < j} d_{ij} \left[ 2\hat{I}_z^i \hat{I}_z^j - (\hat{I}_x^i \hat{I}_x^j + \hat{I}_y^i \hat{I}_y^j) \right]. \quad (3)$$

The coupling constants are

$$d_{ij} = \frac{1}{2} \frac{\gamma^2 \hbar^2}{r_{ij}^3} (1 - 3 \cos^2 \theta_{ij}), \quad (4)$$

with  $\theta_{ij}$  the angle between the vector  $\vec{r}_{ij}$  and the magnetic field direction [61]. In a frame of reference rotating at the Larmor frequency  $\omega_z$  [61], the Hamiltonian of the spin system reduces to  $\hat{\mathcal{H}}_{\text{dd}}$ . This kind of Hamiltonian can also be simulated with quantum gases [62].

In our system, the spins are the protons of polycrystalline adamantane, and we performed all experiments in Dortmund using a home-built solid-state NMR spectrometer with a  $^1\text{H}$  resonance frequency of  $\omega_z = 300$  MHz. As shown in Fig. 1a, the adamantane molecule is nearly spherical and contains 16 protons. The molecules tumble rapidly and isotropically in the solid phase. This fast tumbling averages the intramolecular couplings to zero, but the interaction between the molecules remains. However, the couplings between molecules are averaged to a nonzero value that depends only on the relative position of the molecules to which the spins belong. They are not isotropic, and they have the normal orientation dependence of dipolar couplings of Eq. (4), but the distance vector is between the positions of the molecules, not of the nuclei. “Position” would in fact not be the center of mass of the molecules, but an effective position that is the result of the averaging

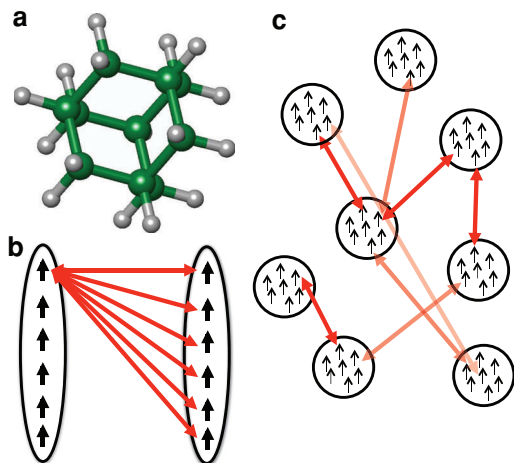


**Figure 1** Spin system. (a) Adamantane molecule with 16 protons (small gray spheres). The large green spheres are mostly  $^{12}\text{C}$  and  $^{13}\text{C}$  in natural abundance (1.1%). (b) The intramolecular interactions are averaged to zero due to very fast molecular tumbling, but the intermolecular interactions average to a nonzero value that depends on the distance between the molecules. The spins interact with spins of the other molecule with the same averaged coupling strength, as shown with arrows. (c) Schematic representation of the interactions between the molecules. The color tones of the arrows represent the variation of the coupling strength with intermolecular distance, which varies as  $1/r_{ij}^3$ .

process. Figure 1b shows a scheme of the interaction between two molecules, where the spins do not interact with spins within a molecule but they interact with all spins of the neighbor molecules. All coupling strength are averaged to the same value. However, in Fig. 1c, the coupling strength between molecules depends on their separation, as shown by arrows with different color tones, and on the polar angle  $\theta_{ij}$  with respect to the magnetic field. The randomness of the dispersion of the distance vector  $\vec{r}$  between molecules will be the source of disorder on  $d_{ij}$ . The molecules are in a face-centered cubic lattice, where each adamantane molecule has 12 first-neighbor interactions with a distance of 6.6 Å, then 6 second neighbors with a distance of 9.34 Å, then 16 at a distance of 11.4 Å, etc. The width of the NMR resonance line is 7.9 kHz.

## 2.2 Preparation of initial state

In NMR experiments, one deals with ensembles of states that are usually described by a density operator. We perform quantum simulations starting from the high-temperature thermal equilibrium [61]. Using the notation  $\hat{I}_z = \sum_i \hat{I}_z^i$ , we can write the density operator of the

thermal equilibrium state as

$$\begin{aligned} \rho_0 &= \exp \left\{ -\frac{\hbar\omega_z}{k_B T} \hat{I}_z \right\} / \text{Tr} \left\{ \exp \left\{ -\frac{\hbar\omega_z}{k_B T} \hat{I}_z \right\} \right\} \\ &\approx \left( \hat{1} + \frac{\hbar\omega_z}{k_B T} \hat{I}_z \right) / \text{Tr} \{ \hat{1} \}. \end{aligned} \quad (5)$$

It is convenient to exclude the unity operator  $\hat{1}$  since it does not evolve in time and does not contribute to the observable signal. The resulting density operator is  $\hat{\rho}_0 \propto \hat{I}_z$ . In this state, the spins are uncorrelated and the density operator commutes with the Hamiltonian  $\hat{\mathcal{H}}_{\text{dd}}$ . In order to prepare a different initial state, we wait a time longer than  $T_1$  to reinitialize the system state to  $\rho_0$ . In the following, when we mention the state of the system, we refer to its density operator unless it is explicitly stated that a different class of state is considered.

## 3 Quantum simulations

### 3.1 Unperturbed evolution

#### 3.1.1 Generating clusters

The initial density operator  $\rho_0$  of the uncorrelated spins commutes with  $\hat{\mathcal{H}}_{\text{dd}}$ . Therefore, to generate spin clusters we use an NMR method developed by Pines and co-workers [64, 65]. It is based on generating an average Hamiltonian  $\hat{\mathcal{H}}_0$  that does not commute with the thermal equilibrium state:

$$\begin{aligned} \hat{\mathcal{H}}_0 &= - \sum_{i < j} d_{ij} [ \hat{I}_x^i \hat{I}_x^j - \hat{I}_y^i \hat{I}_y^j ] \\ &= - \frac{1}{2} \sum_{i < j} d_{ij} [ \hat{I}_+^i \hat{I}_+^j + \hat{I}_-^i \hat{I}_-^j ]. \end{aligned} \quad (6)$$

This Hamiltonian drives an evolution that converts the thermal initial state into clusters of correlated spins whose density operator contains terms of the form  $\hat{I}_u^i \dots \hat{I}_v^j \hat{I}_w^k$  ( $u, v, w = x, y, z$ ), where the indexes  $i, j, k$  identify the spins involved in the given cluster. The cluster size  $K$  corresponds to the number of terms in this product, which is equal to the number of spins. The cluster size is related to the volume occupied by those spins. Experimentally, the Hamiltonian  $\hat{\mathcal{H}}_0$  is generated with the pulse sequence [64, 65] shown in Fig. 2a.

In the usual computational or Zeeman basis  $|\alpha_1, \alpha_2, \dots, \alpha_K\rangle$  ( $\alpha_i = \uparrow, \downarrow$ ) for a system of  $K$  spins, we write the states as  $|M_z, n_M\rangle$ , where  $M_z$  is the total magnetic quantum number, i.e.  $\hat{I}_z |M_z, n_M\rangle = M_z |M_z, n_M\rangle$ , and  $n_M$  distinguishes different states with the same

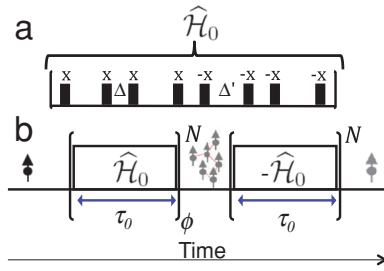


**Figure 2** Pulse sequence for quantum simulations. The effective Hamiltonian  $\hat{H}_0$  is generated by a periodic sequence of  $\pi/2$  pulses. (a) The basic cycle, where  $\Delta' = 2\Delta + \tau_p$ ,  $\Delta = 2\mu\text{s}$ , and  $\tau_p = 2.8\mu\text{s}$  is the  $\pi/2$  pulse duration [65]. The cycle time is then  $\tau_0 = 57.6\mu\text{s}$ . (b) The complete sequence of evolutions.

$M_z$ . Figure 3a shows a summary of these states, whose degeneracy is  $\max\{n_M\} = K! / [(K/2 - M_z)!(K/2 + M_z)!]$ .

The Hamiltonian  $\hat{H}_0$  flips simultaneously two spins, which are separated in space and have the same orientation. Accordingly, the  $z$ -component of the magnetization  $M_z$  changes by  $\Delta M_z = \pm 2$ . This is shown with a curved solid arrow in Fig. 3a. At the same time, the number  $K$  of correlated spins changes by  $\Delta K = \pm 1$ . Therefore, starting from the thermal equilibrium state, the evolution generates a density operator where only elements  $\rho_{ij}$  with  $\Delta M = M_z(i) - M_z(j) = 2n$ ,  $n = 0, 1, 2, \dots$  are populated. Such elements  $\rho_{ij}$  are called  $\Delta M$  quantum coherences and they are represented by colored straight arrows in Fig. 3a. The different colors represent different multiple-quantum coherence (MQC) orders  $\Delta M$ . Off-diagonal elements of the density matrix with  $\Delta M = 0$  represent zero-quantum coherences and diagonal ele-

ments correspond to populations. Then, a MQC spectrum  $A(\Delta M)$  can be described by the number of coherences of the density matrix for a given  $\Delta M$ . A typical MQC spectrum is shown in Fig. 3b. The initial density operator  $\rho_0$  is diagonal and then  $A(\Delta M) \neq 0$  only for  $\Delta M = 0$ . However, as time evolves, different spins interact with each other and other coherence orders are excited. Then  $A(\Delta M)$  starts to spread as a manifestation of the increasing cluster size. If we measure the evolution of the operator  $I_z$  as a function of time,  $\langle I_z(t) \rangle = \text{Tr}\{I_z\rho(t)\}$ , its expectation value decays as a consequence of the excitation of the coherences of the density matrix that do not contribute to the observable  $\langle I_z(t) \rangle$ . The black squares in Fig. 4 show the evolution of  $\langle I_z(t) \rangle$  driven by the Hamiltonian  $\hat{H}_0$ . The data show a fast decay on a time scale of  $\approx 100\mu\text{s}$ , which is followed by a quantum beat at about  $400\mu\text{s}$ . Then the signal saturates at a value of about 4% of the initial value at least up to 2 ms. We expect that it decays at longer times.

### 3.1.2 Measuring cluster sizes

To determine the average number of correlated spins in the generated clusters, we use the NMR technique developed by Baum et al. [65]. In a system of  $K$  spins, the number of transitions with a given  $\Delta M$  follows a binomial distribution

$$n(\Delta M, K) = \frac{(2K)!}{(K + \Delta M)!(K - \Delta M)!} \quad (7)$$

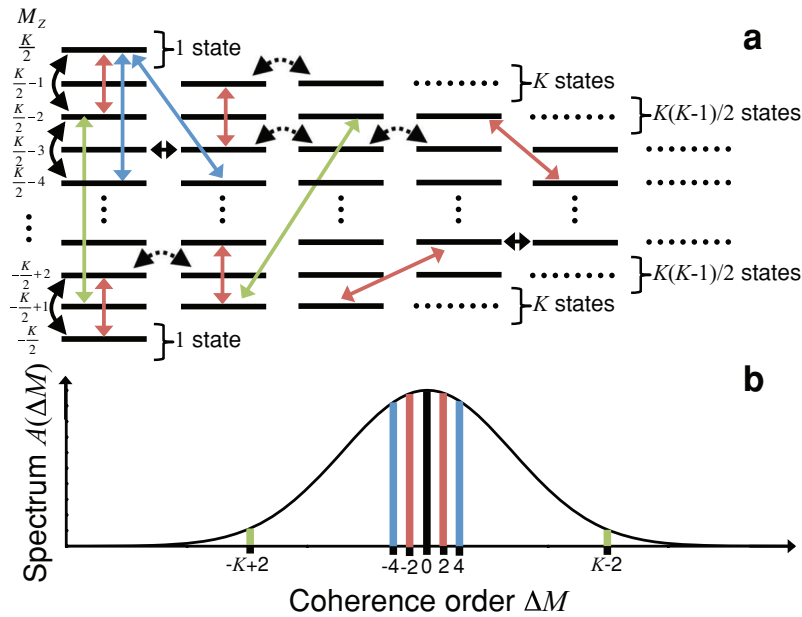


**Figure 3** Energy level scheme for a cluster of  $K$  spins. (a) The different rows correspond to Zeeman states  $|\alpha_1, \alpha_2, \dots, \alpha_K\rangle$  ( $\alpha_i = \uparrow, \downarrow$ ) with different energy determined by the quantum number  $M_z$ . The degeneracy of the levels in a row is given on the right-hand side of each row. The solid curved arrows show those transitions induced by the Hamiltonian  $\mathcal{H}_0$  that do not conserve  $M_z$ . The dotted curved arrows show the effect of the  $M_z$ -conserving dipolar Hamiltonian  $\mathcal{H}_{\text{dd}}$ . The straight colored arrows show the possible coherences generated by  $\mathcal{H}_0$ . (b) The number of coherences of a cluster of size  $K$  is plotted as a function of  $\Delta M$ . The colored bars give those numbers and their color code corresponds to that of (a).

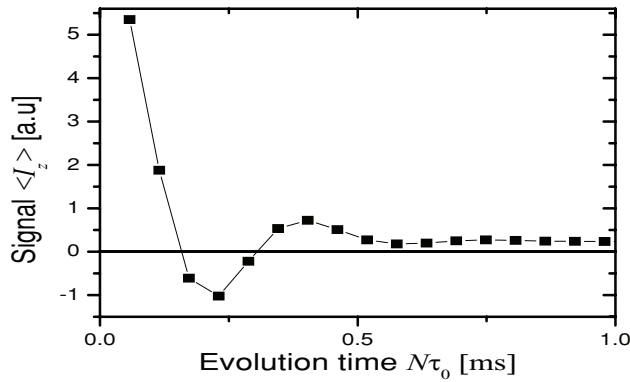


**Figure 4** Time evolution driven by  $\mathcal{H}_0$  of the total magnetization  $\langle I_z(t) \rangle$  of the system as a function of time.

For  $K \gg 1$ , the binomial distribution can be approximated with a Gaussian

$$n(\Delta M, K) \propto \exp\left(-\frac{\Delta M^2}{K}\right), \quad (8)$$

whose half width at  $e^{-1}$  is  $\sigma = \sqrt{K}$ . Thus, the width of the MQC spectrum reflects the cluster size. We can determine the effective size of the spin clusters in a given state by measuring the distribution of the MQCs of its density operator  $\rho$  as a function of the coherence order  $\Delta M$ . They can be distinguished experimentally by rotating the system state around the  $z$ -axis: a rotation  $\hat{\phi}_z = e^{-i\phi \hat{I}_z}$  by  $\phi$  changes the density operator to

$$\hat{\rho}(\phi) = \hat{\phi}_z \hat{\rho} \hat{\phi}_z^\dagger = \sum_{\Delta M} \hat{\rho}_{\Delta M} e^{i\Delta M \phi}, \quad (9)$$

where  $\hat{\rho}_{\Delta M}$  contains all the elements of the density operator involving coherences of order  $\Delta M$ .

By following the sequence of Fig. 2b, the system evolution is first described by an evolution period of duration  $N\tau_0$  under the Hamiltonian  $(\hat{\mathcal{H}}_0)_\phi = \hat{\phi}_z \hat{\mathcal{H}}_0 \hat{\phi}_z^\dagger$ , i.e.

$$\begin{aligned} \hat{\rho}_0 \xrightarrow{(\hat{\mathcal{H}}_0)_\phi N\tau_0} \hat{\rho}_\phi(N\tau_0) &= \hat{\phi}_z \hat{\rho}(N\tau_0) \hat{\phi}_z^\dagger \\ &= \hat{\phi}_z e^{-i\hat{\mathcal{H}}_0 N\tau_0} \hat{\rho}_0 e^{i\hat{\mathcal{H}}_0 N\tau_0} \hat{\phi}_z^\dagger \\ &= \sum_{\Delta M} \hat{\phi}_z \hat{\rho}_{\Delta M}(N\tau_0) \hat{\phi}_z^\dagger \\ &= \sum_{\Delta M} \hat{\rho}_{\Delta M}(N\tau_0) e^{i\Delta M \phi}. \end{aligned} \quad (10)$$

The next part of the sequence of Fig. 2b is an evolution of the same duration  $N\tau_0$  under  $-\hat{\mathcal{H}}_0$ . This causes an evolution backwards in time that gives the following density

operator at the end of the sequence:

$$\begin{aligned} \xrightarrow{(-\hat{\mathcal{H}}_0) N\tau_0} \hat{\rho}_f(2N\tau_0) &= e^{i\hat{\mathcal{H}}_0 N\tau_0} \hat{\rho}_\phi(N\tau_0) e^{-i\hat{\mathcal{H}}_0 N\tau_0} \\ &= \sum_{\Delta M} \left[ e^{i\hat{\mathcal{H}}_0 N\tau_0} \hat{\rho}_{\Delta M}(N\tau_0) e^{-i\hat{\mathcal{H}}_0 N\tau_0} \right] \\ &\quad \times e^{i\Delta M \phi}. \end{aligned} \quad (11)$$

If  $\hat{I}_z$  is the NMR observable, then the signal becomes

$$\begin{aligned} \langle \hat{I}_z \rangle(\phi, N\tau_0) &= \text{Tr} \{ \hat{I}_z \hat{\rho}_f(2N\tau_0) \} \\ &= \text{Tr} \left\{ e^{-i\hat{\mathcal{H}}_0 N\tau_0} \hat{\rho}_0 e^{i\hat{\mathcal{H}}_0 N\tau_0} \hat{\rho}_\phi(N\tau_0) \right\} \\ &= \text{Tr} \{ \hat{\rho}(N\tau_0) \hat{\rho}_\phi(N\tau_0) \} \\ &= \sum_{\Delta M} e^{i\phi \Delta M} \text{Tr} \{ \hat{\rho}_{\Delta M}^2(N\tau_0) \} \\ &= \sum_{\Delta M} e^{i\phi \Delta M} A(\Delta M), \end{aligned} \quad (12)$$

where  $A(\Delta M)$  are the amplitudes of the MQC spectrum shown in Fig. 3b. To extract these amplitudes from the experimental data, we measure the signal  $\langle \hat{I}_z \rangle(\phi, N\tau_0)$  as a function of  $\phi$  at a fixed time  $N\tau_0$  and then perform a Fourier transform with respect to  $\phi$  as shown schematically in Fig. 5. The cluster size is then determined by the half-width at  $e^{-1}$ ,  $\sigma = \sqrt{K}$ , of  $A(\Delta M)$ .

### 3.1.3 Growth of clusters

Figure 6 shows the time evolution of the measured cluster size  $K(N\tau_0)$  as a function of the total evolution time  $N\tau_0$ . For the unperturbed Hamiltonian, the cluster size appears to grow indefinitely [20, 39]. Figure 6 also shows two examples of the  $A(\Delta M)$  distributions at different times. We can see that for long times  $K \propto (N\tau_0)^{4.3}$  (solid red line). The estimated cluster size  $K$  can contain uncertainty. However, the profile of the MQC spectra is the same for the range of times explored in the experiments, and thus we expect only to have a systematic error that could be a multiplicative factor. Then, if we assume that the cluster size  $K$  is associated with the number of spins inside a volume whose size is scaled by an unknown factor of order unity, it is seen that the associated length  $\ell$  grows faster than in the case of normal diffusion, where  $\ell \propto (N\tau_0)^{3/2}$ .

This evolution can be reversed completely by changing the Hamiltonian from  $\hat{\mathcal{H}}_0$  to  $-\hat{\mathcal{H}}_0$ . Experimentally, this is achieved by shifting the phase of all radiofrequency pulses by  $\pm\pi/2$  [64]. The signal  $\langle I_z \rangle(\phi, N\tau_0)$  at the end of the sequence of Fig. 2b is a time reversal

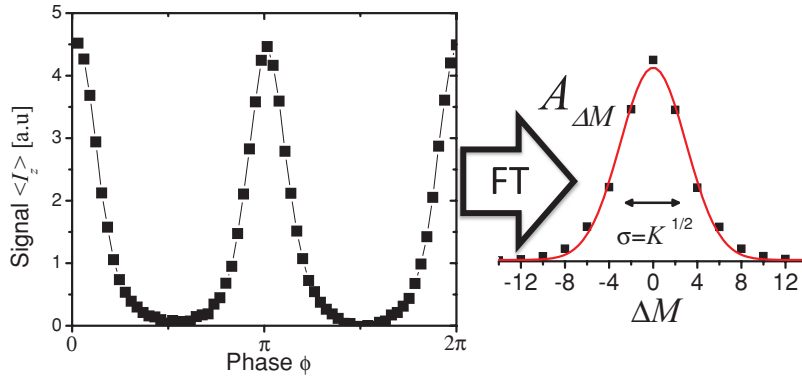


**Figure 5** Scheme for determining the MQC spectrum based on the sequence of Fig. 2. The left-hand panel shows the measured  $\langle I_z \rangle$  signal as a function of the encoding phase  $\phi$  for  $N\tau_0 = 230.4 \mu\text{s}$ . After carrying out a Fourier transform, the MQC spectrum  $A(\Delta M)$  is obtained (right-hand panel). In the left-hand panel, the black squares represent the unperturbed signal ( $p = 0$ ).

echo for  $\phi = 0$ . This means that under ideal conditions  $\sum_M A(\Delta M, N\tau_0)$  is constant and we will write  $E(N\tau_0)$  for this quantity. The indefinite growth of the cluster size as well as the complete reversibility of the time evolution are no longer possible if the effective Hamiltonian deviates from the ideal form Eq. (6).

### 3.2 Effect of perturbations

#### 3.2.1 Intrinsic perturbations

Experimentally, the Hamiltonian  $\hat{H}_0$  is generated as an effective Hamiltonian by the pulse sequence of Fig. 2a. Because of experimental imperfections, it always deviates from the ideal Hamiltonian (Eq. (6)). As a result, the actual dynamics deviates from the ideal one and, in particular, we cannot invert exactly the perturbed Hamiltonian and thus reverse the time evolution perfectly. The quantity  $\sum_{\Delta M} A(\Delta M)$  is no longer conserved, but decays with increasing evolution time. In this section, we study the effects of these imperfections to address the possible impact of them on the quantum simulation of the localization effects.

The ideal form of the effective Hamiltonian of Eq. (6) can only be created if the dipolar couplings  $d_{i,j}$  are time independent and the pulses are ideal and rotate globally all the spins. However, if these couplings are time dependent, or the pulses are not ideal, the effective Hamiltonian (averaged over the pulse cycle) contains additional terms. We have partly characterized the spectral density of local spin–spin fluctuations driven by  $\hat{H}_{\text{dd}}$  in previous work [58, 66] and found a correlation time  $\tau_d = 110 \mu\text{s}$ . Since the imperfections of the generated  $\hat{H}_0$  are driven by  $\hat{H}_{\text{dd}}$ , we can use  $\tau_d$  to estimate the correlation time of these imperfections.

In Fig. 6 the cluster size grows faster for times shorter than  $\tau_d$  (this is best seen in the lower panel). After  $\tau_d$ , the growth of the clusters continues at a slower rate that ap-

pears to become exponential (blue dashed line) [20, 39]. After 1 ms, the growing law again changes its behavior and the cluster size grows as a power law (red solid line) [20, 39]. We cannot contrast this regime with the spectral density determined in previous work [66] because it was not determined for the corresponding range of frequency fluctuations. The exponential growth agrees with the behavior expected from theoretical predictions for this kind of system [67, 68]. The power law behavior may be related to the prediction by Lacelle [69] that after a certain number of spins (around 1000 in adamantane) the effective spin-network topology turns into a three-dimensional spin-coupling network, which leads to a power law growth. The borders between these regimes cannot be rigorously determined. However, the results clearly show that the cluster size keeps growing for a long time, at a rate that is faster than in normal diffusion. This “super-diffusion” deserves further studies since there are no quantum mechanical models describing this behavior and it may be a result of the complex long-range nature of the dipolar interaction in our system [70, 71].

In previous work [20, 39] and in Fig. 6, we determined the cluster growth by isolating the intrinsic decay generated by an imperfect effective Hamiltonian (Eq. (6)). The imperfection effects are manifested in the overall decrease of the echo signal  $E(N\tau_0)$  and we isolated them by normalizing the MQC spectra such that the total signal  $\sum_{\Delta M} A(\Delta M)$  for  $\phi = 0$  is constant in time. Now, we measured the decay of  $E(N\tau_0) = \sum_{\Delta M} A(\Delta M, N\tau_0)$ . The results are shown in Fig. 7. If we consider the imperfections on  $\hat{H}_0$ , the effective Hamiltonian during the first part of the sequence of Fig. 2a will be  $\hat{H}_{\text{fwd}} = \hat{H}_0 + \hat{H}_e$ , and  $\hat{H}_{\text{bwd}} = -\hat{H}_0 + \hat{H}'_e$  during the time-reversed part, where  $\hat{H}_e$  is a representative average error Hamiltonian. The echo decay is then  $E(N_0\tau_0) = \text{Tr} \{ \hat{\rho}^{\hat{H}_{\text{fwd}}}(N\tau_0) \hat{\rho}^{\hat{H}_{\text{bwd}}}(N\tau_0) \}$  and it quantifies the time-reversal probability as a kind of Loschmidt echo [27, 28, 72].

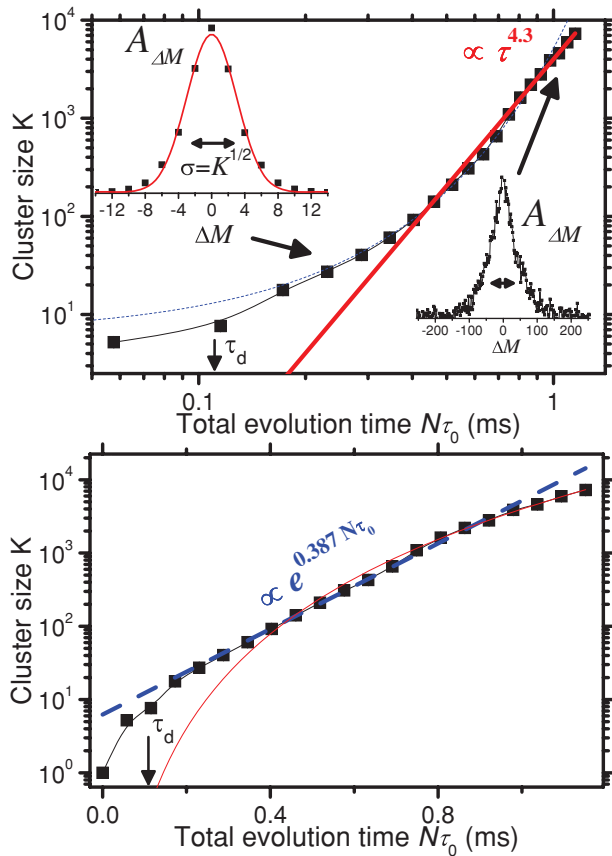


**Figure 6** Time evolution of the cluster size of correlated spins with the unperturbed Hamiltonian  $\hat{\mathcal{H}}_0$  (black squares) for log–log (top) and log–linear (bottom) scales. Distributions of the squared amplitudes  $A_{\Delta M}$  of density operator components as a function of the coherence order  $\Delta M$  are shown for two different cluster sizes. The solid red line is a fitted power law function in the long-time regime and the dashed blue line is an exponential fitted to the range 0.2–0.9 ms.

The echo decay  $E(N_0\tau_0)$  shown in Fig. 7 starts as a Gaussian for times shorter than  $N_0\tau_0 \lesssim 288 \mu\text{s} \approx 2.6\tau_d$ . For longer times it decays exponentially until  $\approx 920 \mu\text{s}$  where a different decay law arises. These transitions between different decay laws seem to be correlated with the growing law transitions discussed in the previous paragraphs. This resembles the typical behavior of nuclear spins of a solution diffusing in an inhomogeneous magnetic field with a given standard deviation [73] or in restricted spaces in the presence of a magnetic field gradient [74]. If the spins only interact with the magnetic field, due to the diffusion process, they feel a different magnetic field at different times causing dephasing of the spin signal. The frequency fluctuations have a correlation time given by the time needed to explore the standard deviation of the changes of the magnetic field that is

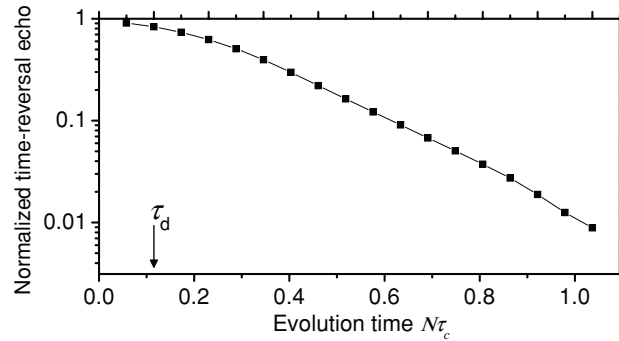


**Figure 7** Time-reversal echo probability. The black squares are the unperturbed ( $p = 0$ ) echo decay  $E(N_0\tau_0)$ , measured with the sequence of Fig. 2, as a function of the evolution time  $N_0\tau_0$ . The  $y$ -axis gives the time-reversal probability normalized with respect to the signal at  $N = 0$ .

related to the inhomogeneity of the magnetic field or to the restriction length. By applying a spin echo sequence – a time reversal of the spin precession by an inversion pulse that changes the sign of the magnetic field interaction – one can partly reverse the effects of the diffusion-driven dephasing [75, 76]. The echo sequence is analogous to that of Fig. 2. If the inversion pulse inducing the time reversal is applied at times shorter than the correlation time of the frequency fluctuations of the spins, the signal decay depends on the spatial displacement of the spins and the signal decays faster as time passes because the dephasing rate increases with the displacement length. However, for times longer than the correlation time of the frequency fluctuations, the decay rate becomes independent of the displacement and becomes exponential, similar to the time-reversal echo behavior shown in Fig. 7.

We clearly see correlations between the characteristic time when the cluster size growing laws (see Fig. 6) and the time-reversal echo decay  $E(N_0\tau_0)$  laws (see Fig. 7) change their behavior compared with the correlation time  $\tau_d = 110 \mu\text{s}$  of the local spin–spin fluctuations driven by  $\hat{\mathcal{H}}_{\text{dd}}$  studied previously [58, 66]. However, we do not observe localization effects generated by the intrinsic imperfections of the generation of  $\hat{\mathcal{H}}_0$  within the dynamic range of evolution times of our experiments. In the following we study the effects of a controlled perturbation proportional to  $\hat{\mathcal{H}}_{\text{dd}}$ , relative to the effects of the intrinsic imperfections of  $\hat{\mathcal{H}}_0$ .

### 3.2.2 Controlled perturbation

The echo decay in Fig. 7 depends on perturbation  $\hat{\mathcal{H}}_e$ . In order to study the sensitivity to the perturbation

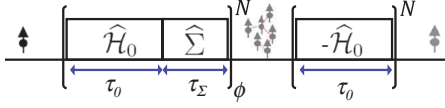


**Figure 8** Sequence for generating a perturbed evolution. It is achieved when  $\tau_\Sigma \neq 0$ , where  $\hat{\Sigma} = \hat{\mathcal{H}}_{\text{dd}}$  is the free evolution Hamiltonian.

strength, we introduce a perturbation  $\hat{\Sigma}$ , whose strength we can control experimentally, and study the behavior of the system as a function of the perturbation strength. We choose the raw dipole–dipole coupling for this perturbation,  $\hat{\Sigma} = \hat{\mathcal{H}}_{\text{dd}}$ , which has long-range interactions with coupling strengths decaying as  $1/r^3$ . We add this Hamiltonian to the ideal Hamiltonian  $\hat{\mathcal{H}}_0$  by concatenating short evolution periods under  $\hat{\mathcal{H}}_{\text{dd}}$  with evolution periods under  $\hat{\mathcal{H}}_0$ . We label the durations of the two time periods  $\tau_\Sigma$  and  $\tau_0$ , as shown in Fig. 8. When the duration  $\tau_c = \tau_0 + \tau_\Sigma$  of each cycle is short compared to the inverse of the dipolar couplings  $d_{ij}$ , the resulting evolution can be described by the effective Hamiltonian

$$\hat{\mathcal{H}}_{\text{eff}} = (1 - p)\hat{\mathcal{H}}_0 + p\hat{\Sigma}, \quad (13)$$

where the relative strength  $p = \tau_\Sigma/\tau_c$  of the perturbation  $\hat{\Sigma} = \hat{\mathcal{H}}_{\text{dd}}$  can be controlled by adjusting the duration  $\tau_\Sigma$ . For the quantum simulations, we compared the artificially perturbed evolution of  $\hat{\mathcal{H}}_{\text{eff}}$  with the  $\hat{\mathcal{H}}_0$  evolution with its intrinsic errors. While the intrinsic errors reduce the signal or the overall fidelity, they do not cause localization on the time scale of our experiments (see Fig. 6).

Starting from thermal equilibrium, now the density operator of the system at the end of  $N$  cycles is  $\hat{\rho}^{\mathcal{H}_{\text{eff}}}(N\tau_c) = e^{-i\hat{\mathcal{H}}_{\text{eff}}N\tau_c} \hat{\rho}_0 e^{i\hat{\mathcal{H}}_{\text{eff}}N\tau_c}$ . Taking into account now the complete sequence of evolutions given by Fig. 8, the experiment is thus a perturbed forward evolution and an unperturbed backward evolution. The density matrix at the end of the sequence is then  $\sum_M \left[ e^{i\hat{\mathcal{H}}_0 N\tau_0} \hat{\rho}_M^{\mathcal{H}_{\text{eff}}}(N\tau_c) e^{-i\hat{\mathcal{H}}_0 N\tau_0} \right] e^{iM\phi}$  as derived previously [20, 39]. Thus the NMR echo signal, which is measured after the last backward evolution  $\exp\{i\hat{\mathcal{H}}_0 N\tau_0\}$ , can be written as

$$\begin{aligned} \langle I_z \rangle(\phi, N\tau_c) &= \text{Tr} \left\{ \hat{I}_z \hat{\rho}_f(N\tau_c + N\tau_0) \right\} \\ &= \text{Tr} \left\{ \hat{\rho}^{\mathcal{H}_0}(N\tau_0) \hat{\rho}_\phi^{\mathcal{H}_{\text{eff}}}(N\tau_c) \right\}. \end{aligned} \quad (14)$$

In terms of the individual MQCs, this may be written as

$$\langle I_z \rangle(\phi, N\tau_c) = \sum_{\Delta M} e^{i\phi \Delta M} \text{Tr} \left\{ \hat{\rho}_{\Delta M}^{\mathcal{H}_0}(N\tau_0) \hat{\rho}_{\Delta M}^{\mathcal{H}_{\text{eff}}}(N\tau_c) \right\} \quad (15)$$

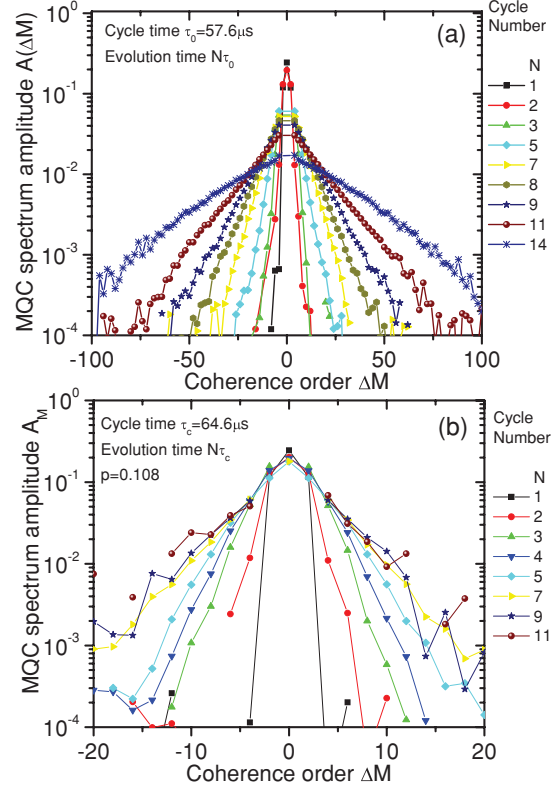


**Figure 9** MQC spectra for different evolution times and perturbation strengths. The  $A(\Delta M)$  spectra (a) for the unperturbed evolution ( $p = 0$ ) for different times and (b) for  $p = 0.108$  for different times. In (b), the width of the MQC spectra remains constant for  $N \geq 7$ , indicating that the spreading of information stops.

with the MQC amplitudes  $A(\Delta M) = \text{Tr} \left\{ \hat{\rho}_{\Delta M}^{\mathcal{H}_0}(N\tau_0) \hat{\rho}_{\Delta M}^{\mathcal{H}_{\text{eff}}}(N\tau_c) \right\}$ . For the ideal evolution ( $p = 0$ ), Eq. (12) is recovered, where  $A(\Delta M)$  correspond to the squared amplitudes of the density operator elements  $\hat{\rho}_{\Delta M}^{\mathcal{H}_0}(N\tau_0)$  with coherence order  $\Delta M$ . For the perturbed evolution ( $p \neq 0$ ), they are reduced by the overlap of the actual density operator elements  $\hat{\rho}_{\Delta M}^{\mathcal{H}_{\text{eff}}}(N\tau_c)$  with the ideal ones. We extract these amplitudes by performing a Fourier transformation with respect to  $\phi$ . Figure 9 shows a comparison between the distributions  $A(\Delta M)$  for different evolution times for an unperturbed evolution (Fig. 9a) and a perturbed evolution with  $p = 0.108$  (Fig. 9b). The main difference is that the MQC spectrum of the perturbed evolution does not spread indefinitely, but its width reaches a limiting value [20, 39].

As discussed in Section 3.1.2, we determine the cluster size for different  $N$  evolution times and perturbation strengths from the width of the measured MQC distributions. Figure 10 shows the cluster size (the number of correlated spins) as a function of the evolution time  $N\tau_c$ . The

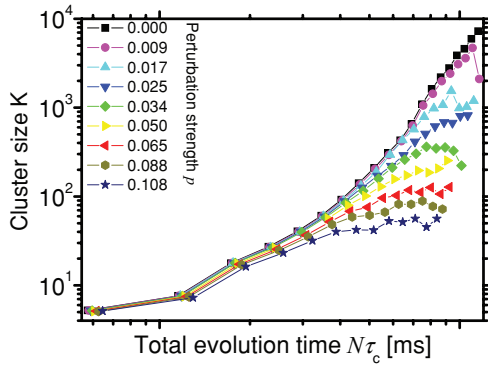


**Figure 10** Time evolution of the cluster size  $K$  for different perturbation strengths. The cluster size is related to the volume occupied by the  $K$  spins. Increasing perturbation strength leads to smaller localization size.

main difference of the perturbed time evolutions (colored symbols in Fig. 10) compared to the unperturbed evolution (black squares) is that the cluster size does not grow indefinitely [20, 39], but saturates. It remains unclear whether the cluster growth for the weakest perturbation  $p = 0.009$  also saturates. We consider this saturation as evidence of localization due to the perturbation and the localization size decreasing with increasing perturbation strength  $p$ .

### 3.3 Quantum dynamics from different initial cluster sizes

We have shown that time evolution of the cluster size under perturbations reaches a dynamical equilibrium state [20, 39], i.e. for a given perturbation strength, the size of the spin clusters tends towards the same limiting value, independent of the initial conditions. In order to show this, we prepared a series of initial conditions corresponding to different cluster sizes. Figure 11 shows the corresponding pulse sequence. The initial state preparation, consisting of an evolution of duration  $N_0\tau_0$  under the unperturbed Hamiltonian  $\hat{\mathcal{H}}_0$ , generates clusters of size  $K_0$ .

During the subsequent perturbed evolution of duration  $N\tau_c$ , these initial clusters evolve and Eq. (14) becomes

$$\langle I_z \rangle(\phi, N_0\tau_0 + N\tau_c) = \text{Tr} \left\{ \hat{\rho}^{\mathcal{H}_0}(N\tau_0, N_0\tau_0) \hat{\rho}_\phi^{\mathcal{H}_{\text{eff}}}(N\tau_c, N_0\tau_0) \right\}. \quad (16)$$

This method allows us to study the growth of the clusters by starting from different sizes  $K_0 = K(N_0\tau_0)$  and fol-

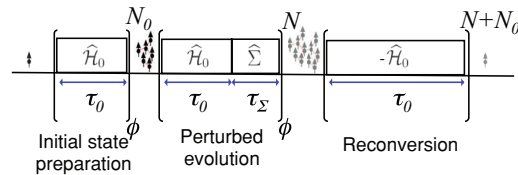


**Figure 11** Sequence for preparing different initial cluster sizes by controlling  $N_0$  and subsequently evolving them in the presence of a perturbation.

lowing the evolution as a function of time and perturbation strength. Based on Eq. (16), we determined the MQC spectra  $A(\Delta M)$  for different evolution times. The insets of Fig. 12 show two examples of them. From such curves, we determined the evolution of the cluster size shown in Fig. 12 (main panel). The figure shows the evolution of the cluster size for two perturbation strengths, starting from different initial sizes. The dynamical equilibrium is clearly manifested in the figure. The two insets show the  $A(\Delta M)$  spectra starting from  $K_0 = 141$ , for different evolution times. We can see that if  $K_0$  is lower than the localization size, then the MQC spectrum spreads until it localizes (manifested by the parallel slopes); however, if  $K_0$  is larger than the localization size, the spectrum shrinks until saturation. We found that the localization size versus the perturbation strength is roughly proportional to  $1/p^2$  [20, 39]. During our experiment, the magnetization is uniform throughout the sample, so the process does not lead to a spatial redistribution of magnetization. Note, however, that here we measure the cluster size of correlated spins that is associated with a coherent length. Therefore, this technique allows investigation of the localization size, even when the magnetization density profile of the excited cluster size exceeds the localization length.

## 4 Conclusions

As a step towards the understanding of the quantum evolution of large quantum systems, we have studied the spreading of information in a system of nuclear spins. Decoherence has long been recognized to limit the time for which quantum information can be used. Spatial disorder also limits the distance over which quantum information can be transferred. We have studied the role of a disordered dipolar interaction Hamiltonian and shown that, for larger values of the perturbation, the coherence length of the cluster size reaches a limit value. Even though we do not measure directly the spatial extent of the cluster size, one might speculate that the spatial

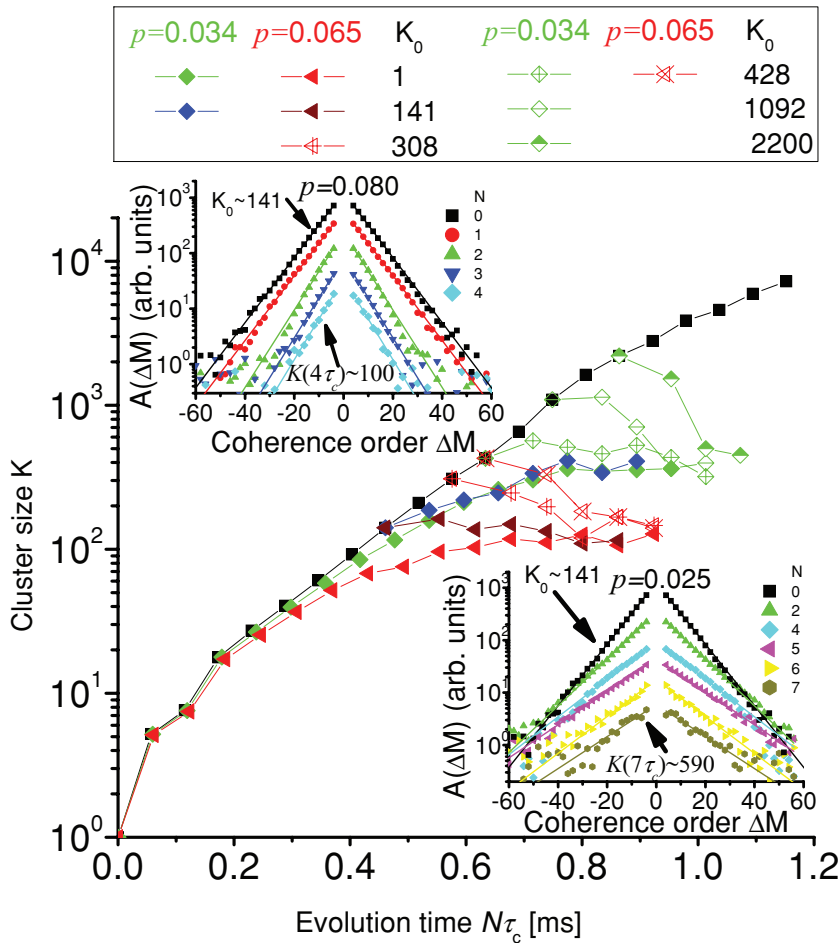


**Figure 12** Time evolution of the cluster size of correlated spins starting from different initial states. The experimental data are shown for two different perturbation strengths given in the legend. The filled black squares, red triangles, and green diamonds are evolutions from an uncorrelated initial state. Open symbols start from an initial state with  $K_0$  correlated spins (see legend). The filled blue diamonds and brown triangles start from an initial  $K_0 = 141$ . The insets show the MQC spectra starting from  $K_0 = 141$  as a functions of time for two perturbation strengths.

extent and the number of correlated spins are related with a volume  $\sim K$ . Investigation of a connection of our results with Anderson localization of spins with dipolar  $1/r^3$  interactions and the interplay with competing interactions could thus be explored [33, 35, 36, 38, 42, 43]. We also note that for lower values of the perturbation, the size of the cluster grows faster than expected for a diffusive model. We will investigate possible connections to Levy flights and Levy walks induced by the long-range dipole–dipole couplings of our Hamiltonians. We developed a method that allows one to quantify the time evolution of the cluster size of correlated spins starting with single qubits. As we have shown, the information can spread to clusters of several thousand qubits. We have observed that the combination of an information spreading Hamiltonian and a perturbation to it results in a quantum state that becomes localized. The localization size decreases with increasing strength of the perturbation and the resulting size appears to be determined by a dynamic equilibrium [20, 39], a feature which might be adapted to other communities studying Anderson localization.

The results presented here provide information about the spatial bounds for transferring quantum information in large spin networks and indicate how precise manipulations of large quantum systems have to be. The sample used in this study can also be an interesting system for studying fundamental aspects of Anderson localization in the presence of long-range interactions.

**Acknowledgments.** This work was supported by the DFG through Su 192/24-1. G.A.A. acknowledges the support of the Alexander von Humboldt Foundation and of the European Commission under the Marie Curie Intra-European Fellowship for Career Development grant no. PIEF-GA-2012-328605.

**Key words.** spin dynamics, dipolar interaction, decoherence, localization, disorder, NMR, long range interactions, quantum information processing.

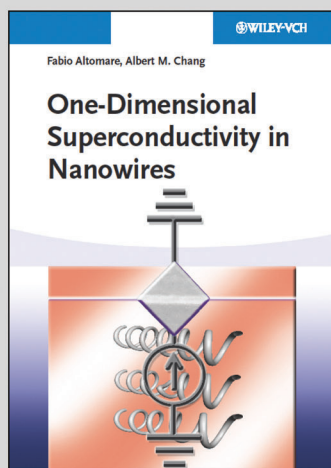
**References**

[1] T. D. Ladd, F. Jelezko, R. Laflamme, Y. Nakamura, C. Monroe, and J. L. O’Brien, *Nature* **464**, 45 (2010).

- [2] D. P. DiVincenzo, *Science* **334**, 50 (2011).
- [3] J. Simon, W. S. Bakr, R. Ma, M. E. Tai, P. M. Preiss, and M. Greiner, *Nature* **472**, 307 (2011).
- [4] A. Aspuru-Guzik and P. Walther, *Nat. Phys.* **8**, 285 (2012).
- [5] R. Blatt and C. F. Roos, *Nat. Phys.* **8**, 277 (2012).
- [6] I. Bloch, J. Dalibard, and S. Nascimbène, *Nat. Phys.* **8**, 267 (2012).
- [7] A. A. Houck, H. E. Türeci, and J. Koch, *Nat. Phys.* **8**, 292 (2012).
- [8] T. Schulz, R. Ritz, A. Bauer, M. Halder, M. Wagner, C. Franz, C. Pfleiderer, K. Everschor, M. Garst, and A. Rosch, *Nat. Phys.* **8**, 301 (2012).
- [9] P. W. Shor, Proceedings of the 35th Annual Symposium on the Foundations of Computer Science, editor edited by S. Goldwasser (IEEE Computer Society Press, Los Alamitos, CA, 1994), p. 124.
- [10] D. P. DiVincenzo, *Science* **270**, 255 (1995).
- [11] M. A. Nielsen and I. L. Chuang, *Quantum Computation and Quantum Information* (Cambridge University Press, Cambridge, 2000).
- [12] P. Hauke, F. M. Cucchietti, L. Tagliacozzo, I. Deutsch, and M. Lewenstein, *Rep. Prog. Phys.* **75**, 082401 (2012).
- [13] T. Monz, P. Schindler, J. T. Barreiro, M. Chwalla, D. Nigg, W. A. Coish, M. Harlander, W. Hänsel, M. Hennrich, and R. Blatt, *Phys. Rev. Lett.* **106**, 130506 (2011).
- [14] H. D. Raedt and K. Michielsen, *Handbook Of Theoretical And Computational Nanotechnology, Quantum and Molecular Computing Quantum Simulations*, (American Scientific Publishers, 2006).
- [15] W. Zhang, N. Konstantinidis, K. A. Al-Hassanieh, and V. V. Dobrovitski, *J. Phys.: Condens. Matter* **19**, 083202 (2007).
- [16] G. A. Álvarez, E. P. Danieli, P. R. Levstein, and H. M. Pastawski, *Phys. Rev. Lett.* **101**, 120503 (2008).
- [17] S. Popescu, A. J. Short, and A. Winter, *Nat. Phys.* **2**, 754 (2006).
- [18] H. G. Krojanski and D. Suter, *Phys. Rev. Lett.* **93**, 090501 (2004).
- [19] H. G. Krojanski and D. Suter, *Phys. Rev. Lett.* **97**, 150503 (2006).
- [20] G. A. Álvarez and D. Suter, *Phys. Rev. Lett.* **104**, 230403 (2010).
- [21] J. W. Britton, B. C. Sawyer, A. C. Keith, C.-C. J. Wang, J. K. Freericks, H. Uys, M. J. Biercuk, and J. J. Bollinger, *Nature* **484**, 489 (2012).
- [22] A. Perdomo-Ortiz, N. Dickson, M. Drew-Brook, G. Rose, and A. Aspuru-Guzik, *Scientific Reports* **2**, 571 (2012).
- [23] S. Boixo, T. F. Rønnow, S. V. Isakov, Z. Wang, D. Wecker, D. A. Lidar, J. M. Martinis, and M. Troyer, arXiv 1304.4595 (2013).
- [24] W. S. Bakr, J. I. Gillen, A. Peng, S. Fölling, and M. Greiner, *Nature* **462**, 74 (2009).
- [25] M. Endres, M. Cheneau, T. Fukuhara, C. Weitenberg, P. Schauß, C. Gross, L. Mazza, M. C. Banuls, L. Pollet, I. Bloch, and S. Kuhr, *Science* **334**, 200 (2011).
- [26] W. H. Zurek, *Rev. Mod. Phys.* **75**, 715 (2003).
- [27] H. M. Pastawski, P. R. Levstein, G. Usaj, J. Raya, and J. A. Hirschinger, *Physica A* **283**, 166 (2000).
- [28] R. A. Jalabert and H. M. Pastawski, *Phys. Rev. Lett.* **86**, 2490 (2001).
- [29] H. Cho, P. Cappellaro, D. G. Cory, and C. Ramanathan, *Phys. Rev. B* **74**, 224434 (2006).
- [30] M. Lovric, H. Krojanski, and D. Suter, *Phys. Rev. A* **75**, 042305 (2007).
- [31] C. M. Sánchez, H. M. Pastawski, and P. R. Levstein, *Physica B* **398**, 472 (2007).
- [32] A. Zwick, G. A. Álvarez, J. Stolze, and O. Osenda, *Phys. Rev. A* **85**, 012318 (2012).
- [33] A. Pomeransky and D. Shepelyansky, *Phys. Rev. A* **69**, 014302 (2004).
- [34] G. D. Chiara, D. Rossini, S. Montangero, and R. Fazio, *Phys. Rev. A* **72**, 012323 (2005).
- [35] J. Keating, N. Linden, J. Matthews, and A. Winter, *Phys. Rev. A* **76**, 012315 (2007).
- [36] C. K. Burrell and T. J. Osborne, *Phys. Rev. Lett.* **99**, 167201 (2007).
- [37] T. Apollaro and F. Plastina, *Open Syst. Inform. Dyn.* **14**, 41 (2007).
- [38] J. Allcock and N. Linden, *Phys. Rev. Lett.* **102**, 110501 (2009).
- [39] G. A. Álvarez and D. Suter, *Phys. Rev. A* **84**, 012320 (2011).
- [40] G. A. Álvarez, E. P. Danieli, P. R. Levstein, and H. M. Pastawski, *Phys. Rev. A* **82**, 012310 (2010).
- [41] A. Zwick, G. A. Álvarez, J. Stolze, and O. Osenda, *Phys. Rev. A* **84**, 022311 (2011).
- [42] P. W. Anderson, *Phys. Rev.* **109**, 1492 (1958).
- [43] P. W. Anderson, *Rev. Mod. Phys.* **50**, 191 (1978).
- [44] H. Hu, A. Strybulevych, J. H. Page, S. E. Skipetrov, and B. A. van Tiggelen, *Nat. Phys.* **4**, 945 (2008).
- [45] J. Chabé, G. Lemarié, B. Grémaud, D. Delande, P. Szriftgiser, and J. C. Garreau, *Phys. Rev. Lett.* **101**, 255702 (2008).
- [46] S. S. Kondov, W. R. McGehee, J. J. Zirbel, and B. DeMarco, *Science* **334**, 66 (2011).
- [47] F. Jendrzejewski, A. Bernard, K. Müller, P. Cheinet, V. Josse, M. Piraud, L. Pezzé, L. Sanchez-Palencia, A. Aspect, and P. Bouyer, *Nat. Phys.* **8**, 398 (2012).
- [48] T. Sperling, W. Bührer, C. M. Aegerter, and G. Maret, *Nat. Photonics* **7**, 48 (2013).
- [49] I. L. Aleiner, B. L. Altshuler, and K. B. Efetov, *Phys. Rev. Lett.* **107**, 076401 (2011).
- [50] L. Viola, E. Knill, and S. Lloyd, *Phys. Rev. Lett.* **82**, 2417 (1999).
- [51] D. A. Lidar, I. L. Chuang, and K. B. Whaley, *Phys. Rev. Lett.* **81**, 2594 (1998).
- [52] J. Preskill, *Proc. R. Soc. Lond. A* **454**, 385 (1998).
- [53] E. Knill, *Nature* **434**, 39 (2005).
- [54] E. M. Fortunato, L. Viola, M. A. Pravia, E. Knill, R. Laflamme, T. F. Havel, and D. G. Cory, *Phys. Rev. A* **67**, 062303 (2003).
- [55] T. Monz, K. Kim, A. S. Villar, P. Schindler, M. Chwalla, M. Riebe, C. F. Roos, H. Haffner, W. Hansel, M. Hennrich, and R. Blatt, *Phys. Rev. Lett.* **103**, 200503 (2009).

- [56] M. J. Biercuk, H. Uys, A. P. VanDevender, N. Shiga, W. M. Itano, and J. J. Bollinger, *Nature* **458**, 996 (2009).
- [57] J. Du, X. Rong, N. Zhao, Y. Wang, J. Yang, and R. B. Liu, *Nature* **461**, 1265 (2009).
- [58] G. A. Álvarez, A. Ajoy, X. Peng, and D. Suter, *Phys. Rev. A* **82**, 042306 (2010).
- [59] A. M. Souza, G. A. Alvarez, and D. Suter, *Phys. Rev. Lett.* **106**, 240501 (2011a).
- [60] A. M. Souza, J. Zhang, C. A. Ryan, and R. Laflamme, *Nat. Commun.* **2**, 169 (2011).
- [61] C. P. Slichter, *Principles of Magnetic Resonance*, 2nd edition (Springer-Verlag, 1992).
- [62] T. Lahaye, C. Menotti, L. Santos, M. Lewenstein, and T. Pfau, *Rep. Prog. Phys.* **72**, 126401 (2009).
- [63] M. Saffman, T. G. Walker, and K. Molmer, *Rev. Mod. Phys.* **82**, 2313 (2010).
- [64] W. Warren, S. Sinton, D. Weitekamp, and A. Pines, *Phys. Rev. Lett.* **43**, 1791 (1979).
- [65] J. Baum, M. Munowitz, A. N. Garroway, and A. Pines, *J. Chem. Phys.* **83**, 2015 (1985).
- [66] G. A. Álvarez and D. Suter, *Phys. Rev. Lett.* **107**, 230501 (2011).
- [67] V. Zdobov and A. Lundin, *J. Exp. Theor. Phys.* **103**, 904 (2006).
- [68] V. E. Zdobov and A. A. Lundin, *Russian J. Phys. Chem. B* **2**, 676 (2008).
- [69] S. Lacelle, *Adv. Magn. Opt. Reson.* **16**, 173 (1991).
- [70] R. Metzler and J. Klafter, *Phys. Rep.* **339**, 1 (2000).
- [71] N. Mercadier, W. Guerin, M. Chevrollier, and R. Kaiser, *Nat. Phys.* **5**, 602 (2009).
- [72] W. K. Rhim, A. Pines, and J. S. Waugh, *Phys. Rev. Lett.* **25**, 218 (1970).
- [73] J. R. Klauder and P. W. Anderson, *Phys. Rev.* **125**, 912 (1962).
- [74] R. P. Kennan, J. Zhong, and J. C. Gore, *Magn. Reson. Med.* **31**, 9 (1994).
- [75] E. Hahn, *Phys. Rev.* **80**, 580 (1950).
- [76] H. Carr and E. Purcell, *Phys. Rev.* **94**, 630 (1954).

## +++ Suggested Reading +++ Suggested Reading +++ Suggested Reading +++



2013. XIV, 258 Pages, Hardcover  
106 Fig. (20 Color Fig.), 2 Tab.  
ISBN 978-3-527-40995-2

Register now for the free  
**WILEY-VCH Newsletter!**  
[www.wiley-vch.de/home/pas](http://www.wiley-vch.de/home/pas)

FABIO ALTOMARE / ALBERT CHANG

## One-Dimensional Superconductivity in Nanowires

The emergence of novel fabrication techniques in the last decade has allowed the fabrication of superconducting nanowires which are 1-dimensional. These nanowires allowed the exploration of a superconducting regime previously not accessible. The nanowires exhibit a variety of behaviors depending on material, size, type of electrical contacts. These behaviors include macroscopic quantum tunneling, superconductor-insulator transition, superconductor-metal transition, anti-proximity effect. The book introduces superconductivity and highlights the key

differences introduced by the 1-dimensionality of the sample under study, compared to conventional 3-Dimensional bulk samples. The focus of the book is the transport in 1-dimensional superconductors. Theories relevant to experiment are described and emphasis placed on experimental results and their connection to the theoretical predictions. The experimental results obtained in the last years are tightly related to the emergence of novel fabrication techniques which are also described.

WILEY-VCH • P.O. Box 10 11 61 • 69451 Weinheim, Germany  
Fax: +49 (0) 62 01 - 60 61 84  
e-mail: [service@wiley-vch.de](mailto:service@wiley-vch.de) • <http://www.wiley-vch.de>

**WILEY-VCH**